Materials Transactions, Vol. 58, No. 9 (2017) pp. 1264 to 1273

Energy Analyses for the Imaging Technique of Bonded Regions and Delaminations in a Thin Plate

Takahiro Hayashi* and Shogo Nakao

Graduate School of Engineering, Kyoto University, Kyoto 615–8540, Japan

Defect imaging by a scanning laser source technique has been theoretically and experimentally investigated for a notch and a wall thinning in a plate. This study discusses the applicability of the imaging technique to bonding regions and delaminations in a thin plate. The variations of flexural wave energy generated at a laser source close to a plate edge, a junction of two thin plates, a bonded region, and a delamination are discussed using the Kirchhoff–Love plate theory and a semi-analytical finite element method. The numerical analyses reveal that the flexural wave energy generated in the vicinity of the reflection objects are significantly different in such a source type as normal loading and dipole loading modeled for elastic wave generations due to ablation and thermo-elastic effects, respectively. In particular, the numerical analyses reveal that the dipole loading is more effective to the imaging because the generation energy significantly varies at the boundaries between bonded and separated regions. Moreover, the images of a plate with a bonded region are obtained using an experimental system in which the thermo-elastic effect is dominant for generating elastic waves, and they exhibit similar tendencies with calculated results.
[doi:10.2320/matertrans.M2017151]

(Received May 12, 2017; Accepted June 27, 2017; Published July 28, 2017)

Keywords: *non-destructive testing, Lamb waves, numerical analysis, scanning laser source technique*

1. Introduction

Material evaluations by noncontact and remote measurements are in great demand in large constructions such as pipes and bridges, and large productions such as aircraft fuselages, wings, and automobile bodies[1–4]. Laser ultrasonics[5–11] is one of the most suitable approaches for such noncontact remote evaluations. In the laser ultrasonics, an ultrasonic pulse in the frequency range of megahertz is typically generated using a pulse laser equipment, and the pulse echo is detected using a laser interferometer. Although the noncontact material evaluation technique is in great demand, it has not been replaced with the conventional contact ultrasonic pulse echo technique. The most crucial problem is caused by the limitation of receiving devices. A laser interferometer can detect elastic waves on a material surface less sensitive than contact piezoelectric devices, and it is strongly affected by the surface conditions such as roughness and inclination because wave detection using laser requires scattered light from the surface.

Therefore, authors[12–16] have studied defect imaging of a plate-like structure using a scanning laser source (SLS) technique, in which only the wave source of a laser irradiation spot is rastered and a receiving spot is fixed. The stable wave detection using a fixed receiver has realized significantly rapid wave measurements and defect imaging even in curved plate-like structures such as pipes.

Moreover, theoretical and experimental studies verified that amplitude and frequency of the received waveforms react sensitively with a crack on the surface or back surface stretching in the thickness direction of a plate in the SLS technique[13–22]. For example, Kromine *et al.*[17] and Sohn and Krishnaswamy[18,19] presented that a surface breaking flow can be detected at a high resolution with amplitude change and frequency change in the SLS measurements. Dixon *et al.*[20] and Clough and Edwards[21,22] showed the phenomena that amplitude increases when the laser source is located in the vicinity of a flaw located at the surface or back surface of a plate and the near-field enhancement is useful for flaw detection. The authors of the current paper also confirmed the amplitude enhancement at a wall thinning by the SLS measurement and verified that a defect image can be obtained by rastering the laser source[12]. Moreover, the authors verified theoretically and experimentally that the energy of flexural vibration also increases when laser is irradiated in the vicinity of notch-type defects and proved that the amplitude enhancement is caused by the interaction of evanescent modes generated at the laser source and the reflective object as defects[14]. This result indicates that the energy enhancement is affected not by the wavelength of the flexural wave but by the dominant range of the evanescent modes and implies that defects can be detected at sufficiently high resolution even in the frequency range lower than megahertz. For example, the authors successfully created images of defects on the back surface of an aluminum alloy plate of 3.0 mm thickness in the frequency range of 6–11 kHz[13,16]. Moreover, the authors demonstrated that defect images can be created even for curved plates such as straight pipes and branched pipes as well as flat plates because the imaging technique precisely uses the energy enhancement of flexural waves generated at a laser source.

These previous studies discussed the imaging technique for a thin plate with thickness reduction or defects. This study investigates the application of the SLS technique to the evaluation of adhesive and delamination regions through the analysis of flexural wave propagation. Adhesive bonding has been widely adopted for automotive steel sheet and airplane dissimilar materials, being expected to replace resistance spot welding and rivet bonding. However, adhesive bonding is still limitedly used and carefully handled because the evaluation technique of the bonding quality has not been established. Delamination appears in a layered plate subjected to an impact load, and it significantly decreases the strength of an aircraft body.

*Corresponding author, E-mail: hayashi@kuaero.kyoto-u.ac.jp

This paper is organized as follows. The following section describes the flexural wave motion generated by laser irradiation based on Kirchhoff–Love plate theory and analyses the effect of generation energy with the type of a laser source, the thickness of a plate, and a reflective plate edge in order to support discussions of energy variation around a bonded region and a delamination in the later sections. In Section 3, flexural wave energy is calculated, using a semi-analytical finite element (SAFE) method[23–27], for different laser source location around a junction where two thin plates merge or one thin plate diverges. Section 4 discusses the energy of the flexural wave generated at a laser source in a plate with a bonded region or a delamination and investigates the possibilities of their evaluation with the SLS technique. Then, the calculation results are verified using the SLS experiments for a plate with a bonded region.

2. Theoretical Descriptions of Flexural Wave in Thin Plates

Lamb waves propagating in an elastic homogeneous plate consists of modes with various wavenumbers at a certain frequency, and the wavenumbers can be derived from the Rayleigh–Lamb equation[28–30]. The wavenumbers are numerically calculated because the Rayleigh–Lamb equation cannot be solved explicitly. However, the approximated solutions of flexural waves can be explicitly obtained in the low frequency-thickness product range based on Kirchhoff–Love plate theory[29,31]. Because the imaging technique using the SLS is effective in the low frequency-thickness product range, the theoretical solutions are beneficial for predicting the flexural wave motions in several cases. This section describes flexural wave generated by laser source and total reflection at a plate edge using the Kirchhoff–Love plate theory before discussing flexural waves at adhesive bonding and delamination.

2.1 Flexural waves generated by laser sources

In the laser ultrasonics, irradiation of laser pulses onto a material generates elastic waves. The generation mechanism is theoretically and experimentally elucidated[5–11]. For large laser pulse power, a force normal to the object surface is dominant due to the effect of plasma emission from a material at a laser spot, as Q_0 in Fig. 1 (a). Although the elastic wave generation by ablation may damage the material surface slightly, it can generate large vibration. For small laser pulse power, laser heating induces local and instantaneous thermal expansion and vibration. Although the vibration energy is smaller than that by laser ablation, it does not damage object surface. The thermo-elastic effect induces in-plane forces parallel to object surface, as P_0 in Fig. 1 (b). Assuming a plane strain condition with uniform physical parameters in the direction normal to a plate cross-section (z direction) in this section, the in-plane forces are dipole loading. In a thin plate, the dipole loading induces the external local moment m_0, as shown in Fig. 1 (c). This study discusses these two laser generation mechanisms; normal loading for the ablation and dipole loading for the thermo-elastic effect.

Currently, we consider flexural waves propagating in an

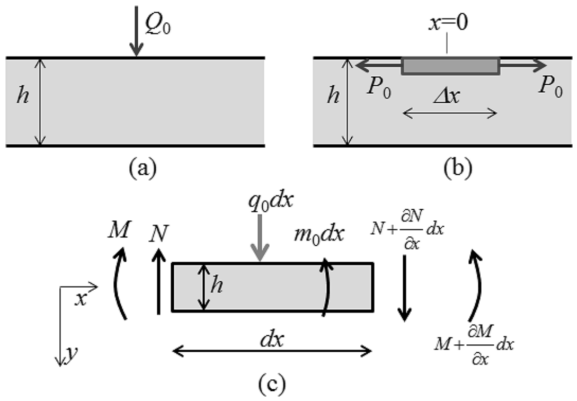

Fig. 1 Schematic figures of external loading for two different types of laser source and forces and moments applied to plate cross-section with infinitesimal length. (a) Normal loading (ablation), (b) Dipole loading (thermo-elastic effect), (c) Element of a plate subjected to forces and moments.

elastic homogeneous plate of thickness h and density ρ, where the propagation direction of the flexural waves and the thickness direction are x and y, respectively. The infinitesimal deflection u is induced by the normal stress q_0 and the external moment per unit area m_0. N and M are the shear force and moment per unit length in the z direction, respectively. The equation of motion in the y direction is expressed as follows[29,31]:

$$\frac{\partial N}{\partial x} + q_0 = \rho h \frac{\partial^2 u}{\partial t^2}. \tag{1}$$

Equilibrium of moment at the left edge provides

$$\frac{\partial M}{\partial x} + m_0 - N = 0, \tag{2}$$

where small terms were eliminated.

Based on the Kirchhoff–Love hypothesis and the assumption of plain strain, the relative equation between the displacement u and the moment M is obtained using the bending stiffness D as follows:

$$M = -D\frac{\partial^2 u}{\partial x^2}, \quad D = \frac{Eh^3}{12(1-\nu^2)}, \tag{3}$$

where E and ν are the Young's modulus and the Poisson's ratio, respectively. From eqs. (1)–(3), the wave equation is expressed as follows:

$$-D\frac{\partial^4 u}{\partial x^4} + \frac{\partial m_0}{\partial x} + q_0 = \rho h \frac{\partial^2 u}{\partial t^2}. \tag{4}$$

When we consider harmonic responses for harmonic load and moment concentrated at $x = 0$ with angular frequency ω ($=2\pi f$: f is frequency), the external stress q_0, moment m_0, and displacement u are expressed as follows:

$$q_0 = Q_0 e^{-i\omega t}\delta(x), \quad m_0 = M_0 e^{-i\omega t}\delta(x), \quad u = U e^{-i\omega t}. \tag{5}$$

In the imaging technique we introduce, harmonic wave analysis is effective because narrowband burst wave is generated by modulating fiber laser emission. The wave eq. (4) becomes

$$-D\frac{\partial^4 U}{\partial x^4} + M_0\frac{\partial \delta(x)}{\partial x} + Q_0\delta(x) = -\rho h\omega^2 U. \tag{6}$$

Taking Fourier transform of eq. (6) yields

$$-Dk^4\bar{U} + iM_0k + Q_0 = -\rho h\omega^2\bar{U}, \tag{7}$$

where $\bar{U}$ is the Fourier transform of U with respect to x, and k is the wavenumber. Rearranging eq. (7) yields

$$\bar{U} = \frac{iM_0k + Q_0}{D(k^4 - k_0^4)}, \tag{8}$$

$$k_0 = \left(\frac{\rho h\omega^2}{D}\right)^{1/4}. \tag{9}$$

From the inverse Fourier transform of eq. (8), the displacement U is expressed as follows:

$$U = \frac{1}{2\pi}\int_{-\infty}^{\infty}\frac{iM_0k + Q_0}{D(k^4 - k_0^4)}e^{ikx}dk. \tag{10}$$

Replacing the infinite integral to a path integral for an appropriate closed path and applying this to the residual theorem provides the following solution:

$$U = \frac{Q_0}{4Dk_0^3}(ie^{ik_0x} - e^{-k_0x}) + \frac{M_0}{4Dk_0^2}(-e^{ik_0x} + e^{-k_0x}), \quad x > 0 \tag{11}$$

where the first and second terms are the contributions of the external concentrated load Q_0 and external moment M_0, respectively.

If we consider the normal loading, as shown in Fig. 1(a), as a model of laser source by ablation where only the first term in eq. (11) is effective, then the displacement can be written as follows:

$$U^{normal} = \frac{Q_0}{4Dk_0^3}(ie^{ik_0x} - e^{-k_0x}), \quad x > 0. \tag{12}$$

In the dipole loading as shown in Fig. 1 (b), allowing the load P_0 and $-P_0$ to be applied at $x = \Delta x/2$ and $x = -\Delta x/2$ on the surface, respectively, the external moments $-P_0\dfrac{h}{2}$ ($\equiv -M_0$) and $P_0\dfrac{h}{2}$ ($\equiv M_0$) are subject at $x = \Delta x/2$ and $x = -\Delta x/2$ on the center of the plate cross-section. Then, the displacement due to the moments is expressed from eq. (11) as follows:

$$\begin{aligned} U^{dipole} = {} & \frac{-M_0}{4Dk_0^2}(-e^{ik_0(x-\Delta x/2)} + e^{-k_0(x-\Delta x/2)}) \\ & + \frac{M_0}{4Dk_0^2}(-e^{ik_0(x+\Delta x/2)} + e^{-k_0(x+\Delta x/2)}), \\ & x > \Delta x/2. \end{aligned} \tag{13}$$

For small $k_0\Delta x$, this equation can be approximated to

$$\begin{aligned} U^{dipole} &\cong \frac{-M_0\Delta x}{4Dk_0}(ie^{ik_0x} + e^{-k_0x}) \\ &= \frac{-P_0\Delta xh}{8Dk_0}(ie^{ik_0x} + e^{-k_0x}), \quad x > \Delta x/2. \end{aligned} \tag{14}$$

Summarizing eqs. (12) and (14), the displacement is expressed as follows:

$$U = C_0(ie^{ik_0x} + S_0e^{-k_0x}), \quad x > \Delta x/2 \tag{15}$$

$$C_0 = \frac{Q_0}{4Dk_0^3}, \quad S_0 = -1, \quad \Delta x = 0, \quad \text{for normal loading} \tag{16}$$

$$C_0 = \frac{-P_0\Delta xh}{8Dk_0}, \quad S_0 = 1, \quad \text{for dipole loading.} \tag{17}$$

The term of e^{ik_0x} in eq. (15) expresses a propagating mode with the wavenumber k_0. Because k_0 provided in eq. (9) is an approximated solution of the A0 mode in the low frequency-thickness product range[29], the term of e^{ik_0x} can be regarded as the A0 mode of the Lamb wave. The term of e^{-k_0x} ($= e^{i(ik_0)x}$) in eq. (15) is a nonpropagating mode that affects in the vicinity of the source, where ik_0 is regarded as the wavenumber of the nonpropagating mode. Because the pure imaginary wavenumber is an approximated solution of the wavenumber of the A1 mode in the low frequency-thickness product range, this term can be regarded as the A1 mode of the Lamb wave. To verify validities of the approximation, Fig. 2 shows the dispersion curves for a plate with thickness h and longitudinal and transverse velocities c_L, c_T = 6300, 3100 m/s, respectively, in the low frequency-thickness product (fh) range. k_{A0} and k_{A1} in the figure are wavenumbers of A0 and A1 modes, respectively, being obtained from Rayleigh-Lamb equation. The dispersion curves denote that k_{A0} and $\mathrm{Im}(k_{A1})$ become closer to k_0 as fh becomes smaller and it can be considered that eq. (15) consists of A0 and A1 modes in the low fh range. Figure 3 shows the displacement distributions for normal and dipole loadings. The horizontal axis is the normalized distance k_0x, and the real parts of the term expressed within parentheses in eqs. (12) and (14) are plotted. In the far field from the source, the curves for both source types are almost identical because only the propagating mode is effective. However, the distributions are significantly different in the vicinity of the source $x = 0$ because the nonpropagating mode e^{-k_0x} affects the near field and the term $S_0e^{-k_0x}$ changes the sign as per the source type.

Subsequently, we consider the vibration energy. The time-averaged vibration energy propagating through the unit length of the z direction towards the $+x$ direction is expressed as follows[31,32]:

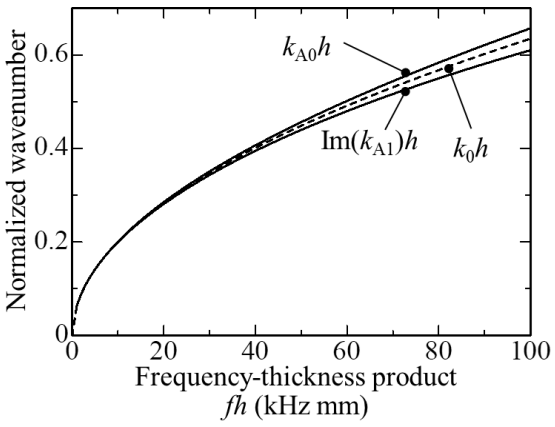

Fig. 2 Dispersion curves obtained from Rayleigh-Lamb equation and eq. (9).

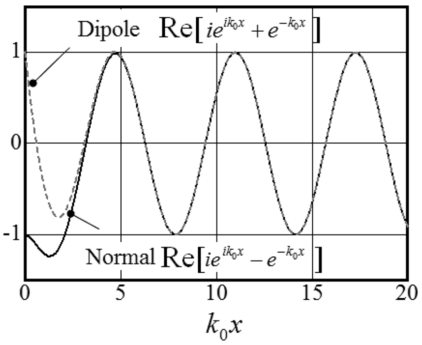

Fig. 3 Displacement distributions for normal and dipole loadings.

$$E = -\frac{1}{2}\mathrm{Re}\left[-M\frac{\partial}{\partial t}\left(\frac{\partial u}{\partial x}\right)^* + N\left(\frac{\partial u}{\partial t}\right)^*\right], \tag{18}$$

where * denotes the complex conjugate. From eq. (2), the first equation of eq. (3), and the third equation of eq. (5), the moment M and the shear force N are expressed in the range except the source point as follows:

$$M = -D\frac{\partial^2 U}{\partial x^2}e^{-i\omega t}, \quad N = -D\frac{\partial^3 U}{\partial x^3}e^{-i\omega t}. \tag{19}$$

Then, eq. (18) can be rewritten as

$$E = -\frac{1}{2}\mathrm{Re}\left[i\omega D\left\{\frac{\partial^2 U}{\partial x^2}\frac{\partial U^*}{\partial x} - \frac{\partial^3 U}{\partial x^3}U^*\right\}\right]. \tag{20}$$

Substituting eq. (15) into eq. (20) yields an equation independent of x as follows:

$$E = \omega D k_0^3 {C_0}^2. \tag{21}$$

Therefore, substituting eqs. (16) and (17) into eq. (21) provides the time-averaged vibration energy for normal loading and dipole loading, respectively, as follows:

$$E^{normal} = \frac{\omega Q_0^2}{16D{k_0}^3}, \quad x \neq 0, \tag{22}$$

$$E^{dipole} = \frac{\omega P_0^2 \Delta x^2 h^2 k_0}{64D}, \quad x > \Delta x/2 \text{ or } x < -\Delta x/2. \tag{23}$$

When the laser irradiation generates elastic waves, Q_0 and $P_0\Delta x$ in eqs. (18) and (19) are constant for constant laser output[5,7]. Therefore, considering $D \propto h^3$ and $k_0 \propto h^{-1/2}$ in the same material, which are expressed in eqs. (3) and (9), the following relations hold at the same frequency and the same laser output.

$$E^{normal} \propto h^{-3/2}, \quad E^{dipole} \propto h^{-3/2} \tag{24}$$

Namely, for both types of laser sources, the time-averaged vibration energy is proportional to $h^{-3/2}$. The relationship between the generation energy and the plate thickness approximately corresponds to the experimental results the authors presented in their previous papers[12].

2.2 Flexural wave reflection at a plate edge

This section discusses the total reflections at the free and fixed edges of a plate as a simple case of reflections based on the Kirchhoff–Love plate theory. We consider the reflection at a plate edge $x = 0$ for a laser source at $x = x_S$, as shown in Fig. 4. Then, from eq. (15), the incident waves by the laser source at $x = x_S$ is written as follows:

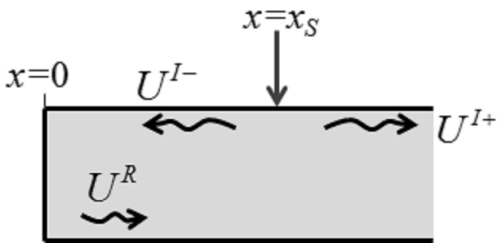

Fig. 4 Reflection at plate edge.

$$U^{I-} = C_0\{ie^{-ik_0(x-x_S)} + S_0 e^{k_0(x-x_S)}\}, \quad x - x_S < -\Delta x/2 \tag{25}$$

$$U^{I+} = C_0\{ie^{ik_0(x-x_S)} + S_0 e^{-k_0(x-x_S)}\} \quad \Delta x/2 < x - x_S. \tag{26}$$

Assuming that the reflected wave is expressed by a linear sum of a propagating mode with e^{ik_0x} and a nonpropagating mode with e^{-k_0x} as

$$U^R = C_1 e^{ik_0x} + C_2 e^{-k_0x}, \tag{27}$$

the following boundary conditions hold at $x = 0$ for a fixed edge where displacement and deflection angle become zero as

$$U^R + U^{I-} = 0, \quad \frac{\partial(U^R + U^{I-})}{\partial x} = 0. \tag{28}$$

The following equations hold at $x = 0$ for a free edge where moment and shear force are zero, from eq. (19), as

$$\frac{\partial^2(U^R + U^{I-})}{\partial x^2} = 0, \quad \frac{\partial^3(U^R + U^{I-})}{\partial x^3} = 0. \tag{29}$$

The coefficients C_1 and C_2 in eq. (27) are determined using these boundary conditions. Using the boundary condition index S_1 that indicates -1 for a fixed boundary condition eq. (28) and $+1$ for a free boundary condition eq. (29), the coefficients C_1 and C_2 are obtained as follows:

$$C_1 = C_0\{-e^{ik_0x_S} + (1-i)S_0S_1e^{-k_0x_S}\}, \tag{30}$$

$$C_2 = C_0\{(i-1)S_1e^{ik_0x_S} - iS_0e^{-k_0x_S}\}, \tag{31}$$

where the source type index S_0 is specified by eqs. (16) and (17), and the boundary condition index S_1 is defined as follows:

$$S_1 = -1 \quad \text{for fixed-edge boundary condition,}$$

$$S_1 = +1 \quad \text{for free-edge boundary condition.} \tag{32}$$

The time-averaged vibration energy of the reflected wave is expressed by substituting the displacement of reflected wave eq. (27) into eq. (20) as follows:

$$E^R = \omega D k_0^3 C_1 C_1^*. \tag{33}$$

Substituting eq. (30), we obtain the energy of the reflected wave as a function of the source location x_S as follows:

$$E^R = E_0[1 - 2S_0S_1e^{-k_0x_S}\{\cos(k_0x_S) - \sin(k_0x_S)\} + 2e^{-2k_0x_S}], \tag{34}$$

where E_0 is expressed as

$$E_0 = \omega D k_0^3 C_0^2. \tag{35}$$

This is nothing but the time-averaged vibration energy in a plate without any reflections, as shown in eq. (21). Figure 5 shows the reflection energy variations with the source location, in which the horizontal axis is the normalized source location k_0x_S and the vertical axis is the normalized vibration energy E^R/E_0. Equation (34) shows two different distributions for the product of indices S_0 and S_1. If the source type is normal loading and the plate edge is a fixed boundary, or if the source type is dipole loading and the plate edge is a free boundary, then $S_0S_1 = +1$ and the reflection energy varies as indicated by the solid line in Fig. 5. On the contrary, if the source type is normal loading and the plate edge is a free boundary or if the source type is dipole loading and the plate edge is a fixed boundary, then $S_0S_1 = -1$ and the reflection energy varies as indicated by the dashed line in Fig. 5. When the source is located far from the plate edge, e.g., $k_0x_S > 6$, $E^R/E_0 = 1$ in both cases. However, when the source is located close to the plate edge, the two curves are significantly different. For $S_0S_1 = -1$, the reflection energy becomes larger as the source is closer to the plate edge. In contrast, for $S_0S_1 = +1$, the normalized reflection energy E^R/E_0 has the maximum point at $k_0x_S \approx 1.3$, and it gradually approaches to $E^R/E_0 = 1$ as k_0x_S becomes smaller. The energy variations in the vicinity of reflective objects, such as in Fig. 5, were also observed for notch-type defects in our previous study[14].

However, one cannot measure only reflected waves at small x_S in actual measurements of reflected waves, and the displacement field can be obtained at $x > x_S$ in the form of interference of reflected wave U^R and incident wave U^{I+} as follows:

$$\begin{aligned} U^R + U^{I+} &= C_1 e^{ik_0x} + C_2 e^{-k_0x} + C_0\{ie^{ik_0(x-x_S)} + S_0 e^{-k_0(x-x_S)}\} \\ &= (C_1 + iC_0e^{-ik_0x_S})e^{ik_0x} + (C_2 + C_0S_0e^{k_0x_S})e^{-k_0x} \\ &\quad x > x_S. \end{aligned} \tag{36}$$

The vibration energy of the interfered wave field is obtained in a similar form of eq. (33) as follows:

$$E^{R\&I+} = \omega D k_0^3 (C_1 + iC_0e^{-ik_0x_S})(C_1 + iC_0e^{-ik_0x_S})^*. \tag{37}$$

Substituting eq. (30) into eq. (37) yields

$$\begin{aligned} E^{R\&I+} = 2E_0[1 &- \sin(2k_0x_S) - 2S_0S_1e^{-k_0x_S}\{\cos(k_0x_S) \\ &- \sin(k_0x_S)\} + e^{-2k_0x_S}]. \end{aligned} \tag{38}$$

Similar to eq. (34), this equation also shows the energy variations with the source location, being plotted in Fig. 6. For large k_0x_S, because $e^{-k_0x_S}$ becomes negligibly small and $E^{R\&I+}$ is approximated to $2E_0\{1 - \sin(2k_0x_S)\}$, $E^{R\&I+}/E_0$ becomes a sinusoidal distribution independent from S_0S_1, with the mean level of 2.0 and with the variation period of $\lambda/2$, where λ is the wavelength of the flexural wave. When a source is located in the vicinity of the plate edge, $E^{R\&I+}$ becomes larger as k_0x_S becomes small for $S_0S_1 = -1$, and $E^{R\&I+}/E_0$ converges to zero for $S_0S_1 = +1$.

3. Energy Analysis for a Plate with a Junction Using a Semi-Analytical Finite Element Method

As the classical plate theory based on the Kirchhoff–Love hypothesis explicitly expresses vibration energy as eqs. (22), (23), (34), and (38), it is considerably effective to analyze the flexural vibration in a plate. However, the classical theory, considering the displacement only in the plate thickness direction, cannot be used when longitudinal vibration such as the S0 mode of the Lamb wave and other higher order modes affect vibration in a plate, which implies that it cannot be applied to partial reflection and transmission at reflective objects such as cracks, defects, delamination, and bonding areas, precisely. Therefore, many theoretical studies were presented to solve the problems. For example, Mindlin derived approximated solutions for Rayleigh-Lamb exact theory that can be applied in higher fh range by considering rotary inertia and shear stresses[33,34]. Rokhlin investigated Lamb wave propagation in a plate with an inner crack with finite width and revealed resonance phenomena due to multiple reflections at the edges of a delamination[35,36]. Moreover, Rokhlin and Bendec theoretically elucidated Lamb wave motions around a junction and a bonded region of two elastic sheets and confirmed turning phenomena at a junction and resonance in a bonded region[37]. However, theoretical treatment generally escalates the complexity as the geometric shape and boundary conditions become complex. Calculation techniques such as finite difference method and finite element method are powerful tools to clarify such

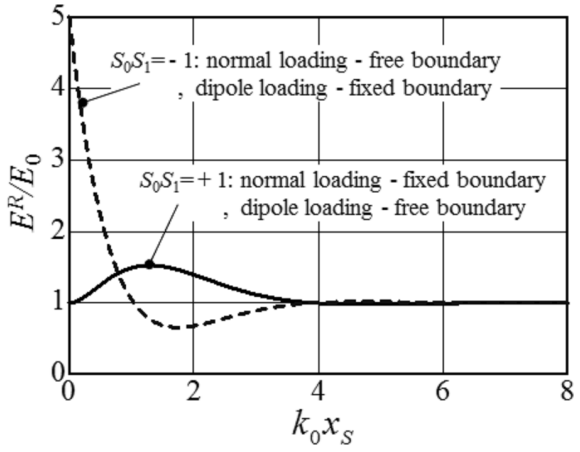

Fig. 5 Reflection energy from plate edge for various source locations.

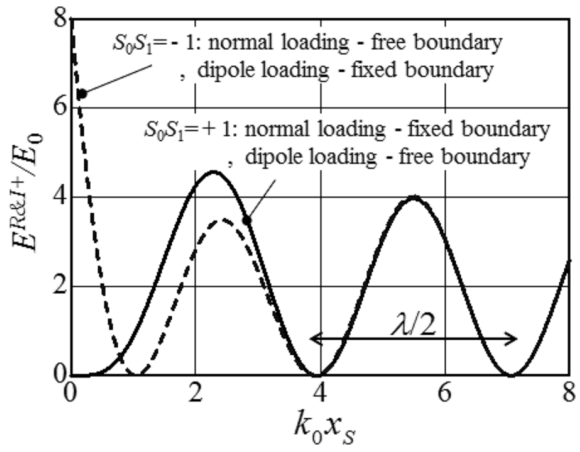

Fig. 6 Total energy at $x < x_s$ for various source locations.

complex wave propagation[23,38,39]. The first author also developed a SAFE method and its combination technique with a finite element method for examining the Lamb wave motion at defects such as cracks and wall thinning[14,24]. Our previous paper[14] discussed the effect of a vertical crack to images obtained in the SLS measurements, in which the vertical crack was expressed by connecting two SAFE regions. Prior to discussing flexural wave around a bonded region and delamination, this section investigates the flexural wave energy generated at a laser source close to a branch junction point of two thin plates.

Figure 7 is a schematic figure of the branch junction part in the SAFE calculations. One plate of thickness h_1 (region 1: $x < 0$) and two thinner plates of thickness h_2 (regions 2 and 3: $x > 0$) connect at $x = 0$. Displacement fields in the regions 1, 2, and 3 were calculated so that the displacements and nodal forces could satisfy their continuities at the junction $x = 0$[14,23,24]. The number of layered elements in region 1 was set to 33, and those in regions 2 and 3 were set to 16. All layer elements had identical thickness, and one layer gap of thickness $h_1/33$ was inserted between regions 2 and 3, resulting in $h_2 = 16h_1/33$. All regions were assumed to be aluminum alloy plates with longitudinal velocity $c_L = 6300$ m/s and transverse velocity $c_T = 3100$ m/s in the calculations shown below.

The time-averaged energy by the waves propagating through the cross-section of a plate of thickness h is expressed by the following form using a velocity vector $\mathbf{v}$ and a stress matrix $\mathbf{T}$[14,28],

$$E = -\frac{1}{4}\left[\int_{-h/2}^{h/2} (\mathbf{v}^* \cdot \mathbf{T} + \mathbf{v} \cdot \mathbf{T}^*) \cdot \hat{\mathbf{x}} dy\right], \tag{39}$$

where $\hat{\mathbf{x}}$ is a unit vector normal to the cross-section through which the vibration propagates. Figure 8 shows the variations of energy traveling toward the $-x$ direction in region 1 (E_1) and traveling toward the $+x$ direction in region 2 (E_2) for various source locations x_S. The energies E_1 and E_2 are obtained as eq. (39) by integrating over the cross-section with thickness of h_1 and h_2 respectively and normalized by E_{01} and E_{02} in the graph, where E_{01} and E_{02} are the time-averaged cross-sectional energies propagating in one direction in a plate of thickness h_1 and h_2, respectively, without any reflective objects for the same incident conditions: (a)–(d) for normal loading; (e)–(h) for dipole loading; (a), (c), (e), (g) for E_1/E_{01}; (b), (d), (f), (h) for E_2/E_{02}; (a), (b), (e), (f) for $fh_1 = 10$ kHz mm; and (c), (d), (g), (h) for $fh_1 = 50$ kHz mm.

E_1/E_{01} (Fig. 8(a), (c), (e), (g)) at $x_S/h_1 < 0$ are approximately sinusoidal curves with an amplitude of approximately 0.5, a mean level of 1.0, and a period of $\lambda_{A0-1}/2$, where λ_{A0-1} is the wavelength of the A0 mode in region 1. However, E_2/E_{02} (Fig. 8(b), (d), (f), (h)) at $x_S/h_1 > 0$ are curves with a mean level of approximately 1.3 and with a period of $\lambda_{A0-2}/2$, where λ_{A0-2} is the wavelength of the A0 mode in region 2. These results denote that the energy variations are caused by the interferences between the reflected waves at the junction and the incident wave propagating away from the junction, which corresponds to the results in the total reflection at a plate edge, as shown in Fig. 6, in the previous section. The difference in the mean level between E_1/E_{01} and E_2/E_{02} is caused by the difference in the reflection level at the junction. Namely, the reflection is small when waves travel from the thick region 1 to the thin region 2. In contrast, the reflection becomes larger when the waves transmit from the thin region 2 to the thick region 1. Moreover, in all cases, when the laser source is located at the thin region 2 ($x_S/h_1 > 0$), the mean level of energy becomes larger. This corresponds to eq. (24), in which the flexural wave energy becomes larger for a thinner plate.

Similar sinusoidal curves can be seen at $x_S/h_1 > 0$ in Fig. 8 (g). The curve in this region indicates the variations of transmitted energy and a period of the curve is slightly larger than the wavelength of A0 mode in the region 2 (λ_{A0-2}).

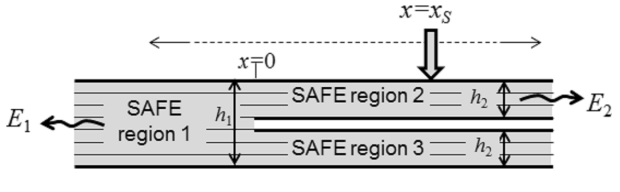

Fig. 7 Schematic figure of the junction of three SAFE regions.

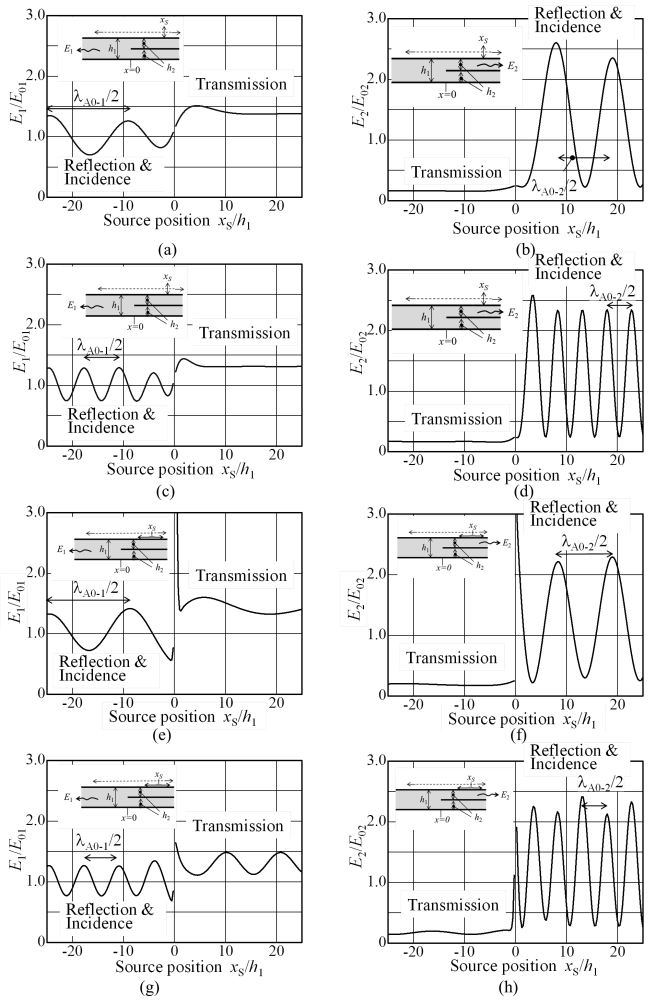

Fig. 8 Variation in elastic wave energy generated for various source locations. (a) E_1, normal loading, $fh_1 = 10$ kHz mm, (b) E_2, normal loading, $fh_1 = 10$ kHz mm, (c) E_1, normal loading, $fh_1 = 50$ kHz mm, (d) E_2, normal loading, $fh_1 = 50$ kHz mm, (e) E_1, dipole loading, $fh_1 = 10$ kHz mm, (f) E_2, dipole loading, $fh_1 = 10$ kHz mm, (g) E_1, dipole loading, $fh_1 = 50$ kHz mm, (h) E_2, dipole loading, $fh_1 = 50$ kHz mm.

Therefore, we cannot conclude the reason of the periodical variation only from the result. It would be consequences of phase of the incident wave at the junction as well as transmitted wave in region 1 and reflected wave in region 3.

Comparing these curves in the source types, the energy variations are significantly different in the vicinity of $x_S/h_1 = 0$. For normal loading, the energy varies continuously at $x_S/h_1 = 0$, whereas, for dipole loading, the energy variations become discontinuous at $x_S/h_1 = 0$. For example, if we carefully observe E_2 ((b), (d), (f), (h)) at the source location of $x_S/h_1 > 0$, the energy E_2 becomes small around $x_S/h_1 = 0$ for normal loading ((b), (d)), but considerably large at $x_S/h_1 = 0$ for dipole loading ((f), (h)). These calculation results agree well with the theoretical solutions for the total reflection, as shown in Fig. 6, if the junction $x_S/h_1 = 0$ is regarded as a fixed boundary. The difference of energy variation in the source types around $x_S/h_1 = 0$ corresponds to the effect of the S_0S_1 term in eq. (38) that is caused by the interference between an evanescent mode generated at a laser source, the term of $e^{k_0(x-x_S)}$ in eq. (25), and an evanescent mode generated at the boundary, the term of $e^{-k_0 x}$ in eq. (27).

4. Energy Analysis for a Plate with a Bonded Region and a Delamination

This section discusses the flexural wave energy generated by laser around a bonded region and a delamination. These structures consist of two junctions that were discussed in the previous section. Bonded regions and delaminations were modeled by the combinations of SAFE regions and a finite element (FE) region. Figure 9(a) is the bonded region model expressed by four SAFE regions and one FE region, and Fig. 9(b) is the delamination model by two SAFE regions and one FE region. The SAFE regions and the FE region were divided into elements at regular intervals in the thickness direction, where the numbers of elements are 33 for thickness h_1 and 16 for thickness h_2. In Fig. 9(a), one layer gap is inserted between the SAFE regions 1 and 2, and the SAFE regions 3 and 4. In Fig. 9(b), small elastic coefficients were set to the center layer in the FE region to model a layer gap of the delamination. The widths of the FE region $w = h_1$, $5h_1$, and $10h_1$ were considered, where the numbers of elements in the width direction were 30, 150, and 300, respectively.

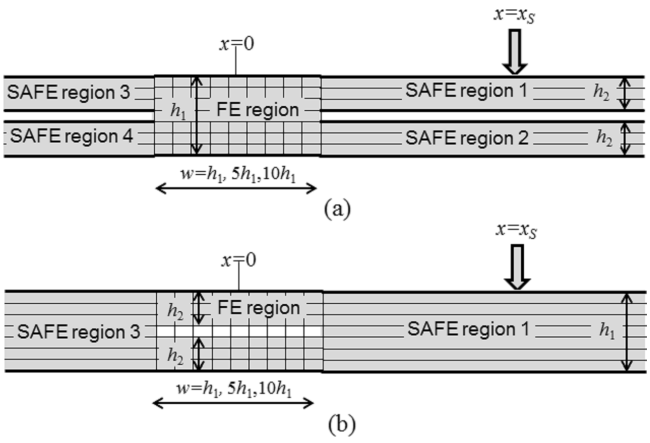

Fig. 9 Calculation regions in the SAFE and FE combined method. (a) Bonded region model, (b) Delamination model.

Figure 10 shows the variations of the energy propagating towards the $+x$ direction in the SAFE region 1 in Fig. 9(a) (E_1) for various source locations x_S around a bonded region. The energy E_1 is normalized by E_{01}, that is, the energy propagates in one direction in a plate of thickness h_1 without any reflective objects under the same generation conditions. The bonded regions are shown in gray, where the center of the regions are $x = 0$. Figure 10 shows the variations in the energy generated around a bonded region at two different frequencies $fh_1 = 10$ kHz mm ((a) and (c)) and $fh_1 = 50$ kHz mm ((b) and (d)), and for two source types of normal loading ((a) and (b)) and dipole loading ((c) and (d)). All curves at the right regions of the gray zones $x_S/h_1 > w/(2h_1)$, indicating the energies generated at the right regions and propagated towards the right direction, are caused by the interferences between the incident wave from the source and the reflected waves at the bonded region because they have a period of $\lambda_{A0-1}/2$. The mean levels at the right regions were larger than the energy levels of the gray bonded regions. This phenomenon roughly agrees with eq. (24) in which larger energy is generated at a thinner plate. The curves at the left regions show the energies transmitted through the bonded regions for a laser source at the left region 3. The transmitted energies are slightly larger than the energies at the gray bonded regions, which are also caused by the phenomena that the flexural wave energy generated is smaller at the bonded region.

Comparing normal and dipole loadings, the energy variations at the boundaries are significantly different; the energy curves vary continuously at the boundaries between the bonded region and the separation regions in normal loading, while the energy curves vary discontinuously at the bound-

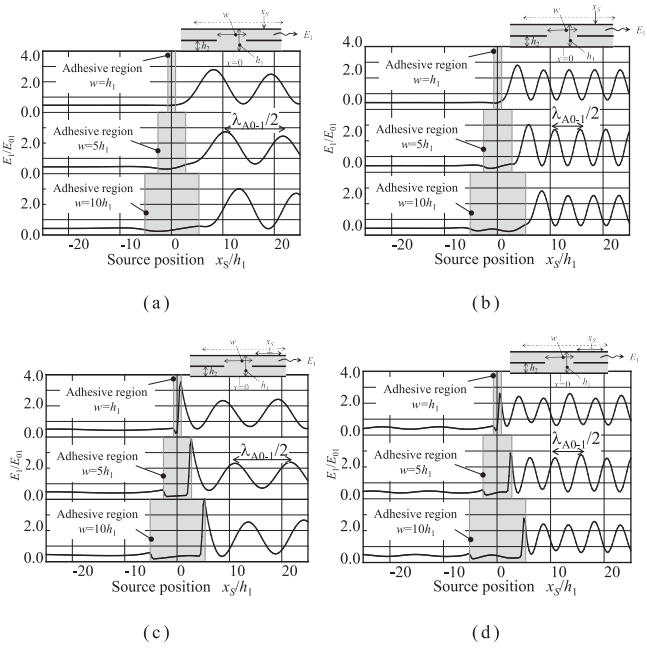

Fig. 10 Variation in elastic wave energy generated for various source locations around a bonded region. (a) $fh_1 = 10$ kHz mm, normal loading, (b) $fh_1 = 50$ kHz mm, normal loading, (c) $fh_1 = 10$ kHz mm, dipole loading, (d) $fh_1 = 50$ kHz mm, dipole loading.

aries in dipole loading. In particular, significant energy change is observed at the right boundary in dipole loading. This abrupt change in energy was also observed for a junction in Fig. 8.

Figure 11 shows the variations of energy propagating in a plate with a delamination towards the $+x$ direction for a laser source located at various positions x_S. The energy E_1 is normalized by E_{01}, that is, the energy generated and propagated in an infinite plate with the same thickness (h_1). The energy curves were calculated at two different frequency-thickness products and for two types of laser sources.

In the case of small width $w = h_1$, E_1/E_{01} is approximately 1.0 at any source positions because waves transmit through the small delamination without reflections at both frequency-thickness products and for both source types. We can understand this phenomenon qualitatively by considering longitudinal waves through two parallel boundaries of semi-infinite media and a thin plate. When the plate inserted between two semi-infinite media is infinitely thin, the reflection at the boundaries becomes zero. A small delamination of $w = h_1$ also did not affect the reflection and transmission like the longitudinal wave at the infinitely thin plate. In the case of $w = 5h_1$ and $10h_1$, the energies vary due to reflections at the delamination. As seen in Fig. 8 and Fig. 10, the energy varies at a period of $\lambda_{A0-1}/2$ in the region 1 showing the interference between incident wave and reflected wave. The energy variations are continuous at the left and right boundaries of the delamination ($x_S = \pm w/2$) for normal loading in Fig. 11(a) and (b), while the energy variations abruptly change at the boundaries for dipole loading in Fig. 11(c) and (d). These energy variations also correspond to those in Fig. 8 where the curves were continuous at the junction for normal loading and discontinuous for dipole loading.

Considering the above-mentioned results, we can conclude that the dipole loading is more effective for detecting a bonded region and a delamination because distinct energy variations can be obtained at boundaries between bonded and separated regions.

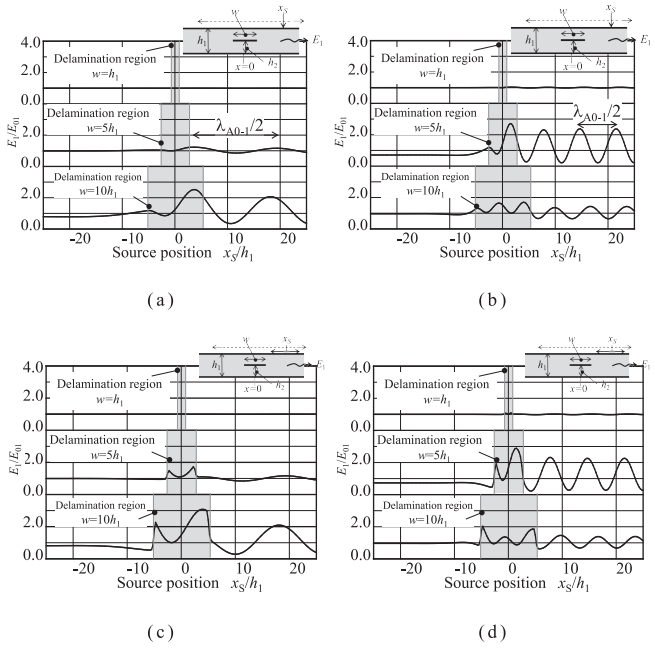

Fig. 11 Variation in elastic wave energy generated for various source locations around a delamination region. (a) fh_1 = 10 kHz mm, normal loading, (b) fh_1 = 50 kHz mm, normal loading, (c) fh_1 = 10 kHz mm, dipole loading, (d) fh_1 = 50 kHz mm, dipole loading.

5. Experimental Verifications by Imaging Bonded Regions

In this section, the calculation results discussed earlier are verified using the SLS imaging experiments for a bonded plate. Figure 12 shows the experimental setup and the specimen used. Because the experimental system is the same as that in our previous studies[14–16], it is briefly described in this section. The fiber laser equipment of 50 W and 1070 nm irradiated laser pulses at the repetition rate of 580 kHz, and the laser pulses were modulated by 5-kHz and 6-cycle rectangular burst signals. This resulted in the generation of 5-kHz and 6-cycle burst elastic waves in the test plate. The laser from the fiber laser equipment was focused on the plate surface using a collimator and a focusing lens. The laser spot was rastered at 2-mm increment over the region of 200 mm × 100 mm (101 × 51 grid points). Because the laser burst trains were irradiated at the repetition frequency of 20 Hz, it required approximately 1/20 Hz × 101 × 51 = 260 s to complete the measurements. The elastic waves were received by a piezoelectric device with the nominal frequency of 4.0 kHz attached on the plate surface at the center of the right edge. The signals received were amplified at 60 dB

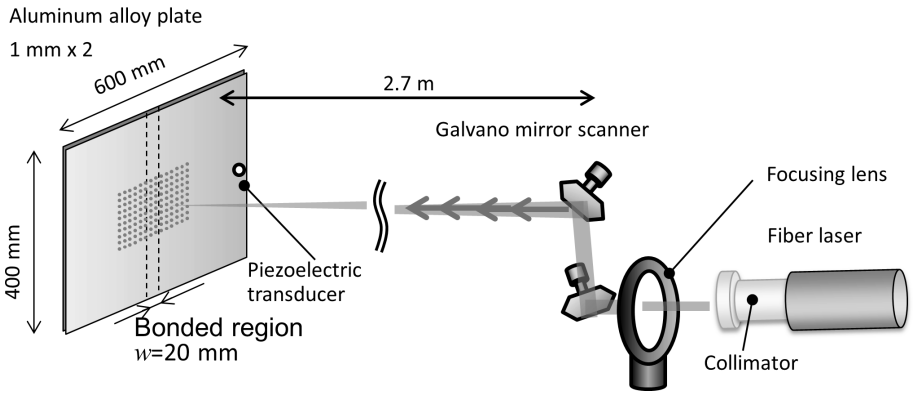

Fig. 12 Experimental setup and a test plate.

and the digitized waveforms in 3 ms were recorded. The test plate is shown in Fig. 12; two aluminum alloy plates with dimensions 600 mm × 400 mm × 1 mm were adhered by epoxy adhesive at the center band of w = 20 mm, as indicated by dashed lines on the plate in Fig. 12.

Because the laser output is not considerably high as to damage the plate surface due to ablation, the thermo-elastic effect, i.e., dipole loading, is dominant in the elastic wave generation. In the experiments, the laser beam was focused to a small circular spot and the radial stress generates axisymmetrically, which is not exactly equivalent to the dipole loading we discussed so far. However, the experimental results can be discussed qualitatively by comparing with the calculation results Fig. 10 (c) for the dipole loading and for the bonded region as shown in Fig. 9 (a).

Fourier spectra of the received signals were calculated, and the peak values of the Fourier spectra at 5 kHz were normalized by the maximum value and were plotted for rastering positions in gray scale as shown in Fig. 13. A straight light gray band of width 20 mm can be clearly observed at the center of the image, which indicates that the energy generated at the bonded region and reached the receiving device was small. In particular, the boundaries between the bonded region and the separated regions can be distinctly observed due to discontinuity of the distribution. Moreover, vertical striped patterns are observed in the right separated region. Because the wavelength of the A0 mode in a 1-mm-thick aluminum plate is approximately 45 mm at 5 kHz, the wavy patterns are about a half period of the wavelength of the A0 mode, indicating the interference between incident wave and reflected wave. The black and gray lines in Fig. 14 are the distribution of the peak values at the horizontal centerline of Fig. 13 and the calculation results shown in Fig. 10 (c). This figure clearly shows these features of the distribution; i.e. abrupt change at the boundaries and periodical variation with $\lambda_{A0\_1}/2$. Although the experimental amplitude gradually decreases from the right to the left due to the diffusion and attenuation, these features of the distribution agree well with the calculation result, which depict that the calculation results obtained are valid and the imaging technique using the SLS is beneficial for bonded regions.

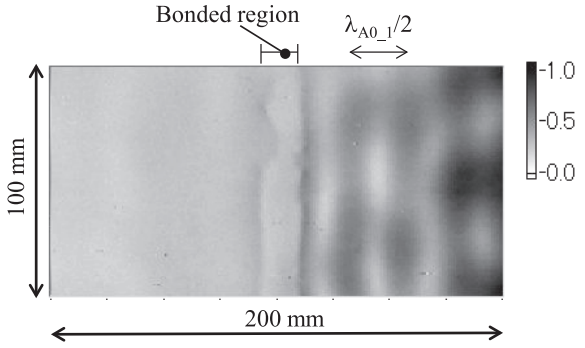

Fig. 13 Distribution of frequency spectra peak value for rastering positions.

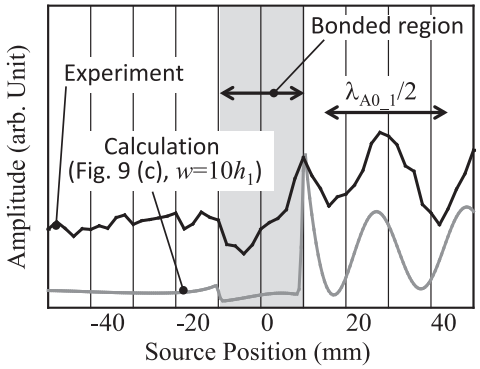

Fig. 14 Comparison of the distributions. The experimental line is the peak distribution at the horizontal centerline of Fig. 13, and the calculation line is in Fig. 9 (c), $w = 10h_1$.

6. Conclusions

Flexural wave energy generated by laser was examined using the Kirchhoff–Love plate theory and a SAFE method in order to investigate the application of the SLS technique to imaging of bonded regions and delaminations in plate structures. First, the theoretical solutions for flexural wave energy reveal that the energies generated in both source types, normal loading and dipole loading, are proportional to $h^{-3/2}$, where h is the plate thickness. Theoretical solutions also revealed that the energy reflected at a plate edge varies with the source type when a laser source is located close to the plate edge. Subsequently, flexural wave energies generated in a plate with a junction, a bonded region, or a delamination were calculated using the SAFE. The calculation results showed a decrease in the generation energy when a laser source is located at a thick bonded region. Moreover, the energy variations were caused by the interference between incident and reflected waves. For dipole loading, the generation energy varies discontinuously at the boundaries between bonded and separated regions, which imply that a bonded region and a delamination can be detected more distinctly for the dipole loading. In the SLS experiment, the image of a bonded region provided similar results with the calculated results; this experimental result revealed that the imaging technique using the SLS is beneficial for the bonded region.

Acknowledgments

This work was supported by JSPS KAKENHI Grant Number 26282094 and 17H02052.

REFERENCES

1) M. Palaniappan, R. Subbaratnam, A. Baskaran and R. Chandramohan: Int. J. Press. Vessels Piping **73** (1997) 33–37.
2) H.A. Kishawy and H.A. Gabbar: Int. J. Press. Vessels Piping **87** (2010) 373–380.
3) P. Cawley: Compos. **25** (1994) 351–357.
4) L.J. Jacobs and R.W. Whitcomb: J. Nondestruct. Eval. **16** (1997) 57–65.
5) C. B. Scruby and L. E. Drain: Laser Ultrasonics: Techniques and Applications (Adam Hilger, New York, 1990), Chap. 5, 223–324.
6) J.-C. Cheng and Y.H. Berthelot: J. Phys. D Appl. Phys. **29** (1996) 1857–1867.
7) J.D. Achenbach: J. Mech. Phys. Solids **51** (2003) 1885–1902.
8) I. Arias and J.D. Achenbach: Int. J. Solids Struct. **40** (2003) 6917–

6935.
9) Y. Shi, S.-C. Wooh and M. Orwat: Ultrasonics **41** (2003) 623–633.
10) J.D. Achenbach: J. Acoust. Soc. Am. **116** (2004) 1481–1487.
11) D.A. Hutchins, R.J. Dewhurst and S.B. Palmer: Ultrasonics **19** (1981) 103–108.
12) T. Hayashi, M. Murase and M.N. Salim: J. Acoust. Soc. Am. **126** (2009) 1101–1106.
13) T. Hayashi: Appl. Phys. Lett. **108** (2016) 081901.
14) T. Hayashi and M. Fukuyama: J. Acoust. Soc. Am. **140** (2016) 2427–2436.
15) T. Hayashi and K. Ishihara: Ultrasonics **77** (2017) 47–53.
16) T. Hayashi: NDT Int. **85** (2017) 53–62.
17) A.K. Kromine, P.A. Fomitchov, S. Krishnaswamy and J.D. Achenbach: Mater. Eval. **58** (2000) 173–177.
18) Y. Sohn and S. Krishnaswamy: J. Acoust. Soc. Am. **115** (2004) 172–181.
19) Y. Sohn and S. Krishnaswamy: Meas. Sci. Technol. **17** (2006) 809–818.
20) S. Dixon, B. Cann, D.L. Carroll, Y. Fan and R.S. Edwards: Nondestruct. Test. Eval. **23** (2008) 25–34.
21) A.R. Clough and R.S. Edwards: NDT Int. **62** (2014) 99–105.
22) A.R. Clough and R.S. Edwards: Ultrasonics **59** (2015) 64–71.
23) G.R. Liu, Z.C. Xi, K.Y. Lam and H.M. Shang: J. Appl. Mech. **66** (1999) 898–903.
24) T. Hayashi and K. Kawashima: Ultrasonics **40** (2002) 193–197.
25) T. Hayashi, K. Kawashima, Z. Sun and J.L. Rose: J. Acoust. Soc. Am. **113** (2003) 1241–1248.
26) T. Hayashi, W.-J. Song and J.L. Rose: Ultrasonics **41** (2003) 175–183.
27) T. Hayashi, C. Tamayama and M. Murase: Ultrasonics **44** (2006) 17–24.
28) B. A. Auld: Acoustic fields and waves in solids II (2nd ed. Krieger, Malabar, 1990) Chap. 10, 63–220.
29) K. F. Graff: *Wave Motion in Elastic Solids*, (Dover, New York, 1991) Chaps. 3, 4 and 7, pp.140–272, 394–581.
30) J. L. Rose, Ultrasonic Waves in Solid Media (Cambridge University Press, New York, 1999) Chap. 8, 101–131.
31) C.H. Wang and L.R.F. Rose: J. Sound Vib. **264** (2003) 851–872.
32) A.N. Norris and C. Vemula: J. Sound Vib. **181** (1995) 115–125.
33) C.D. Mindlin: J. Appl. Mech. **18** (1951) 31–38.
34) C.D. Mindlin: J. Appl. Phys. **22** (1951) 316–323.
35) S.I. Rokhlin: J. Acoust. Soc. Am. **67** (1980) 1157–1165.
36) S.I. Rokhlin: J. Acoust. Soc. Am. **69** (1981) 922–928.
37) S. Rokhlin and F. Bendec: J. Acoust. Soc. Am. **73** (1983) 55–60.
38) K. Harumi: NDT Int. **19** (1986) 315–332.
39) R.L. Datta, S.K. Shah, A.H. Bratton and T. Chakraborty: J. Acoust. Soc. Am. **83** (1988) 2020–2026.